Ductile deformation during carbonation of serpentinized peridotite

Manuel D. Menzel[1]*, Janos L. Urai[1], Estibalitz Ukar[2], Greg Hirth[3], Alexander Schwedt[4], András Kovács[5], Lidia Kibkalo[5], Peter B. Kelemen[6]

[1] *Tectonics and Geodynamics, RWTH Aachen University, Lochnerstrasse 4-20, D-52056 Aachen, Germany*

[2] *University of Texas at Austin, Bureau of Economic Geology, TX, USA*

[3] *Brown University, Department of Earth, Environmental and Planetary Sciences, Providence, RI, USA*

[4] *RWTH Aachen University, Central Facility for Electron Microscopy, Aachen, Germany*

[5] *Ernst Ruska-Centre for Microscopy and Spectroscopy with Electrons, Forschungszentrum Jülich Jülich, Germany*

[6] *Lamont–Doherty Earth Observatory, Columbia University, USA*

* corresponding author (manuel.menzel@emr.rwth-aachen.de)

Abstract

Carbonated serpentinites (listvenites) in the Oman Ophiolite record mineralization of several GT of CO_2, but the mechanisms providing permeability for continued reactive fluid flow are unclear. Samples of the Oman Drilling Project show that listvenites with a penetrative foliation have abundant microstructures related to crystal growth and indicate that the carbonation reaction occurred during tectonic deformation. Folded magnesite (magnesium carbonate) veins mark the onset of carbonation, followed by deformation during growth of magnesite. Undeformed magnesite overgrowths and euhedral quartz growth zoning indicate that deformation stopped when the reaction was completed. We propose deformation by dilatant granular flow and dissolution-precipitation assisted the reaction, while deformation in turn was localized in the weak reacting mass. Lithostatic pore pressures promoted this process, creating dilatant porosity for CO_2 transport and solid volume increase. This feedback mechanism may be common in subduction zones, allowing intense fluid-rock interaction in mantle rocks.

Introduction

Carbonated ultramafic mantle rocks occur at the plate interface in subduction zones where mantle rocks come in contact with CO_2-rich fluids. Listvenites – fully carbonated peridotites mostly composed of Mg-rich carbonate minerals and quartz [1] – have attracted attention owing to their potential as a natural analogue for carbon storage applications [2, 3], and because they offer an opportunity to study fluid mass transfer and deformation processes acting at the leading edge of the mantle wedge [4].

Deformation can greatly influence fluid-rock interactions, and altered rocks are far more abundant in tectonically active than in quiescent zones. Thermo-hydro-mechanical-chemical (THMC) processes of coupled fluid flow, large-scale metasomatism and deformation are common in extensional detachments, oceanic transform faults and the plate interface of subduction zones [5, 6, 7, 8]. Here, fluid flow is often closely linked to deformation, forming hydrated assemblages in shear zones (e.g., [9, 10]). The presence of aqueous fluids can enhance deformation by lowering effective stress, allowing dilatancy and activation of dislocation creep as well as pressure solution at high water activities [11, 12, 13, 14]. Yet, because coupled deformation and fluid-rock interactions occur at multiple scales and involve nonlinear coupling of deformation, fluid flow and chemical reactions over time scales that are difficult to investigate in the laboratory, such interactions can be difficult to elucidate.

Listvenites commonly occur along major shear zones or faults that can act as fluid conduits (e.g. [15, 16, 17, 18, 19]), but to what extent deformation plays a role in the progression of carbonation reactions is poorly constrained. The formation of listvenite requires intense and prolonged fluid flow that adds about 30 wt% CO_2 to the rock (e.g., [16, 20]). Even for unusually high CO_2 contents in aqueous fluids (on the order of 1 wt%), this amount of carbonation requires time-integrated fluid rock ratios > 30. Carbonation and serpentinization reactions involve an increase in solid volume by up to 68%[21, 22, 23, 24], which may lead to clogging of pore spaces and decreasing permeability with reaction progress. This effect, in combination with the formation of reaction rims at reaction fronts that can inhibit continued diffusion-limited reaction, is the main reason why carbonation is inferred to be self-limiting in many experiments [25, 26, 27]. In natural settings such as the Oman ophiolite, where massive carbonation of peridotite to listvenite went to completion across volumes on the order of 1 – 2 km^3 [18], tectonic stress and related deformation may play a key role in maintaining sufficiently high permeability to allow the complete carbonation of Mg-silicate reactants. Possible positive feedback mechanisms of deformation on permeability and reactivity in natural shear zones include: (i) grain size reduction and related increase in reactive surface area [13], (ii) creep cavitation during viscous grain boundary sliding and pressure solution [28], (iii) dilatancy during granular flow [29], and (iv) rapid fluid transport along fractures [30, 31]. Listvenites contain a rich variety of (micro)structures, such as preserved reaction fronts, a multitude of veins, and growth zoning in magnesite due to variable redox conditions during reaction progress [16, 20, 32]. Detailed study of the textural evolution over time can shed light on the relationship between carbonation reaction progress and tectonic processes.

The Oman ophiolite hosts the largest and best exposed listvenite occurrences on Earth ([18], and references therein), offering a unique opportunity to study large-scale CO_2-fluid-rock interactions in mantle rocks. The Oman ophiolite has been drilled during the Oman Drilling Project (OmanDP), an international endeavor to obtain a systematic sampling of key sections of the oceanic lithosphere from crust to the basal thrust. Of the various OmanDP drill sites, Hole BT1B aimed to improve our understanding of mass transfer along the shallow subduction interface and uptake of carbon by the overriding mantle wedge [32]. Hole BT1B provided an unprecedented high-quality sample set of carbonated mantle rocks unaffected by surface weathering, which allows targeted sampling for systematic microstructural assessment.

In this study we analyze the temporal evolution of microstructures in the listvenites to better understand the interaction between changing rheology, external stress, and fluid flow during progressing carbonation of peridotite. We use optical and electron microscopic, multiscale imaging and analysis to study the temporal relationships between phase changes and rock fabrics associated with the carbonation processes. Our analysis indicates syn-carbonation brittle and ductile deformation and creation of inter- and intra-granular porosity, which, together with the abundant veins present in these rocks, contributed to the permeability network that allowed progression of carbonation.

Results

Geological background

Listvenites crop out as large (decameter-scale) bands in serpentinite at the base of the Oman ophiolite (Fig. 1). Hole BT1B of the Oman Drilling Project (International Continental Drilling Project Expedition 5057-4B) recovered 196 m of listvenite and serpentinite, and, separated by a fault, 104 m of the underlying metamorphic sole (Fig. 1d) [32]. The presence of quartz-serpentine intergrowths, recrystallization microstructures of quartz and chalcedony after opal, and a nearly complete lack of talc suggest temperatures of 80 – 150 °C during listvenite formation [18]. Low temperatures are supported by intergrown hematite and graphite or amorphous carbon, which require < 200 °C to coexist in equilibrium[33]. Clumped isotope thermometry points to temperatures from 45±5 to 247±52°C for carbonate precipitation in listvenite and serpentinite [18, 34], consistent with the inferences from mineral parageneses. The pressure of listvenite formation is poorly constrained, with a possible range from ~ 0.3 GPa (for 8 – 10 km ophiolite thickness and based on data from autochthonous carbonates below the ophiolite) [35] to the peak depth recorded by the metamorphic sole (0.8 – 1.2 GPa [36]). An internal Rb-Sr isochron with an age of 97 ± 29 Ma [18] suggests that listvenite formation may have been concurrent with subduction of the Arabian margin and/or subsequent ophiolite obduction (97 – 74 Ma; e.g., [37]). The likely source of CO_2-bearing fluids are meta-sedimentary rocks similar to those of the underlying Hawasina Formation (Fig. 1), consistent with a warm, shallow subduction setting [18, 33].

Structural core logging and microstructural investigation of cross-cutting relationships reveal a multi-stage evolution of deformation and fluid-rock interaction in listvenites and serpentinites from Hole BT1B [32]. Many of the listvenites and serpentinites sampled by this core have been deformed and overprinted by post-listvenite cataclasis and faults [38], which has obscured pre- and syn-carbonation textures that can be used to investigate the types of processes leading up to and acting during carbonation. Here we focus on segments of the core that are not overprinted by post-listvenite cataclasites.

Serpentinite - the starting material

Serpentinites in drill core show a range of commonly observed mesh and bastite textures as well as serpentine veins, typical of hydrated mantle peridotite [39, 40]. Relict olivine or pyroxene are absent in serpentinite in drill core and in ~ 1 to 10 m serpentinite reaction zones surrounding listvenite in outcrops, but relicts of primary Cr-spinel are common. Locally, mesh cells are flattened and delineated by Fe-oxides, defining a foliation (Fig. 2 a). Localized deformation of serpentinite in some shear zones produced a strong shape preferred orientation (SPO) and crystallographic preferred orientation (CPO) of serpentine (Fig. 2 b), in which mesh structures are completely obliterated by medium- to fine-grained serpentine. In these shear zones, electron backscatter diffraction (EBSD) analysis indicates that lizardite/chrysotile predominates, while antigorite is rare. Moderately coarse lizardite shows undulose extinction, deformation lamellae and kinking, whereas fine-grained serpentine develops along grain boundaries of coarser crystals as well as within aligned bands (Fig. 2 c).

Such textures are indicative of grain size reduction during intense deformation [41, 42]. Locally, serpentine veins and tabular serpentine aggregates are folded (Supplementary Fig. S5). Cr-spinel in carbonate-bearing serpentinite (ophicarbonate) is commonly fragmented and partially replaced by Fe-chromite or carbonate. Anastomosing carbonate veins resemble an S-C fabric with the primary vein orientation parallel to serpentine cleavage planes (Fig. 1g). Locally the carbonate veins are associated with elongated Fe-oxides aligned (sub)parallel to the veins, and narrow, branched quartz veins (1 – 50 µm) intercalated between serpentine cleavage planes.

Listvenite

Listvenite in core from Hole BT1B consists of magnesite, quartz, and minor relict Cr-spinel, Fe-oxides and, locally, chromian muscovite [32]. Dolomite is the dominant carbonate mineral in a few core intervals, and in listvenite bands north of Site BT1 [18, 32]. In polished wadi outcrops and in core, listvenites can be macroscopically massive or foliated (Fig. 1, Supplementary Fig. S1). Microscopically, most of the BT1B listvenites are characterized by a high density of early, subparallel carbonate veins, which commonly define the macroscopic foliation. In the listvenite matrix between early carbonate veins, two microstructures are common: (i) spheroidal / ellipsoidal to euhedral magnesite in a finer-grained quartz or quartz-chalcedony groundmass, and (ii) magnesite-quartz intergrowths that resemble the protolith serpentinite mesh microstructure. Locally, this matrix has a penetrative foliation oblique to the preferred orientation of early veins.

Foliation in listvenite matrix

Penetrative-foliated listvenites containing folded and transposed veins are most evident in 25 m – 67 m and 188 m – 197 m depth intervals of Hole BT1B (Fig. 1). These foliated listvenites constitute ~10 % (13/115) of the studied listvenite thin sections, and are present in mm-scale shear zones in 3 additional samples (Supplementary Table S1). At the microscale, the foliation is defined by clusters of elongated magnesite ellipsoids (Fig. 1j), and/or aligned magnesite dendrites, hematite grain aggregates (Supplementary Fig. S13), and carbonate vein fragments. SEM-EDS mapping and SEM-cathodoluminescence (CL; Methods) show that in many cases, ellipsoidal magnesites have an Fe-rich core and concentric compositional zoning of Fe, Mg, Mn and Ca contents and variable abundance of silica inclusions (Fig. 1 j & k). A similar magnesite zoning is also common in non-foliated listvenite [34]. In 3D, micro-CT shows that magnesite ellipsoids are oblate in the foliation plane (Supplementary Fig. S6). EBSD analysis shows that in some samples with an SPO of magnesite, quartz also has a weak SPO (Supplementary Fig. S11).

In foliated listvenites, the foliation wraps around relict Cr-spinel porphyroclasts, which occasionally form boudins or have sigmoidal strain shadows marked by hematite grain aggregates. Fig. 3 shows a boudinaged Cr-spinel with magnesite single crystals in the boudin necks and Fe-magnesite in the interstices between partially rotated spinel fragments. The magnesite orientation in the boudin neck is distinct from the preferred orientation of magnesite ellipsoids in the matrix. Magnesite has abundant low-angle grain boundaries (Fig. 3 g); fibrous aggregates that are typical of strain shadows [43] are not evident. Magnesite in the boudin neck has a patchy luminescence that is different from the concentric core-rim zonation of magnesite ellipsoids (Fig. 3 d). The boudin neck magnesite contains a narrow, Fe-rich zone (dark in the CL image) overgrown by a rim of bright luminescent, Si inclusion-bearing magnesite (arrows in Fig. 3 b, c & d). This rim is similar to the partly dendritic rims that mark the transition between magnesite ellipsoids and interstitial quartz elsewhere in the sample (Fig. 1j). Compositional maps and CL images further reveal that Fe-magnesite cores of matrix grain aggregates occasionally form sigma-clasts (yellow arrows in Fig. 3 c & d), with a sense of shear consistent with that of transposed Fe-magnesite veins in the same sample (see below; Supplementary Fig. S9).

Crystallographic preferred orientations in listvenite

Listvenites with a SPO of magnesite ellipsoids have a weak but statistically significant CPO of magnesite, with c-axes oriented perpendicular to the magnesite grain elongation direction in thin section (Fig. 4). Poles to a- and m-planes show a weak girdle distribution (Supplementary Figs. S8 – S19). This CPO and grain elongation relationships are consistent between samples, and are also apparent for fine-grained, dendritic magnesite in the matrix of some foliated listvenites (Fig. 4). In the same samples, quartz locally has a CPO (Fig. 4) with their c-axes parallel to the magnesite SPO, and with weak maxima of poles to a- and m-planes (Supplementary Figs. S8 – S19).

Folding and transposition of early veins

In many of the samples with a penetrative foliation, early antitaxial to blocky magnesite veins are folded and/or transposed (Fig. 5). Foliated zones with folded veins in places have sharp transitions to non-foliated, mesh-textured listvenite zones where veins are not folded. In folded areas, dendritic magnesite shows a strong SPO approximately parallel to the fold axial planes (Fig. 5 a & d) defining an axial planar cleavage. In some fold hinges, quartz shows a CPO with c-axes parallel to the axial planar cleavage (Fig. 5; Supplementary Fig. S16). Fold microstructures are complex due to crosscutting and variable orientations of the early vein generations, transposition of vein fragments, and because folded and transposed veins are overgrown by a later generation of brown, locally euhedral magnesite (Fig. 5 a, d). Optical-CL imaging shows that bright pink-luminescent magnesite overgrowths on folded veins are highly irregular in thickness and transition into axial planar dendritic grains (white arrows in Fig. 5 b), which suggests that this magnesite formed during or after folding. In contrast, dull-luminescent magnesite in vein centers displays comparatively continuous thicknesses and sharp contacts with the matrix. These relationships are more complex around fold hinges, where folded veins coalesce and increase in thickness. Veins commonly have a narrow, bright-luminescent centerline rich in Fe-oxide and/or –hydroxides (Fig. 5 b) and compositional zoning that traces the shape of the folds. The folded zoning and centerline often have small offsets close to fold hinges (Fig. 5 d), even though no faults are visible in the listvenite matrix. In offsets of transposed veins, dendritic magnesite overgrowths are oriented subparallel to oblique to the matrix foliation (Fig. 5c).

Low-angle grain boundaries

Magnesite in folded veins commonly shows similarly oriented domains over relatively long distances despite folding, and abundant low-angle grain boundaries (< 10° misorientation) at high angles to the vein margins and subparallel to the axial planar cleavage (Fig 5 e). In the matrix of foliated listvenite, low-angle boundaries are common in ellipsoidal magnesite, and present but less abundant in quartz (Supplementary Fig. S11). Continuous low-angle boundaries that segment grains into subgrains commonly have traces at high angles to the magnesite SPO, but can also be parallel (Fig. 6 a). Radial, discontinuous low-angle boundaries are common in magnesite ellipsoid rims (Supplementary Fig. S14).

A TEM image of a low-angle boundary in ellipsoidal magnesite is shown in Fig. 6 b. Compositional mapping by STEM reveals that magnesite is Fe-bearing and contains abundant Si-bearing inclusions (20 – 150 nm). Along the low-angle boundary there is an inclusion-free rim of Fe-poor magnesite on both sides of the boundary. A 10 - 20 nm wide Fe-enriched seam occurs along the comparatively straight and sharp contact between the inclusion-free rims and the host magnesite. The actual crystallographic low-angle boundary (bg* in Fig. 6) is rough on the nm-scale. These observations suggest that the crystallographic misorientation across this low-angle boundary is due to a 500 – 600 nm wide intra-granular nano-fracture that was sealed by epitaxial precipitation of inclusion-free magnesite onto the walls. In a few places along the boundary, porosity caused by growth misfit is preserved. Despite the significant abundance of low-angle boundaries and misorientations within magnesite, the dislocation density appears to be generally low, with minor dislocations concentrated at low-angle boundaries that lack inclusion-free magnesite precipitates (not shown in the figure).

Crystal growth microstructures

Foliated listvenites preserve abundant microstructures related to crystal growth, such as growth zoning in quartz and magnesite, euhedral overgrowths of magnesite crystals, and dendritic magnesite rims intergrown with quartz. Listvenites also preserve ubiquitous intra-granular nano- and micro-porosity and locally abundant inter-granular macroporosity.

SEM-CL imaging reveals concentric zoning in magnesite ellipsoids, locally with euhedral growth zones (Fig. 1 j; Fig. 7). The outermost rim of many ellipsoids is dendritic, composed of magnesite-quartz intergrowths. Magnesite dendrites extend into the surrounding quartz (Fig. 7 a). In some areas, the quartz that surrounds magnesite ellipsoids is massive or featureless under SEM-CL, but locally contains dark-luminescent, rounded domains that do not correspond with grain boundaries. In others, quartz clearly envelops magnesite ellipsoids and shows oscillatory and/or sector growth zoning with euhedral growth facets and remarkable dark-luminescent marker zones that can be correlated across crystals (Fig. 7 a). In places quartz shows botryoidal, concentric growth zoning (Fig. 7 b), with spherulitic domains at the transitions into brighter-luminescent zones. CL zoning of quartz indicates heterogeneous crystallization [44]. Apart from veins, quartz does not cut the CL zoning of magnesite, but is intergrown with the delicate magnesite dendrites at the ellipsoid rims. Similar dendritic magnesite occurs on the outer rim of folded magnesite veins, and, in places, on straight crystal facets of euhedral magnesite grains (Fig. 7 c - f). Crystallographic orientations are commonly the same as the larger grains (Fig. 7 d), pointing to epitaxial growth.

Micro-CT indicates that the matrix of foliated listvenites contains ~0.23 % preserved porosity, mostly at rims of magnesite ellipsoids (c.f. Fig. 1 k). Dendritic intergrowths locally contain high inter-granular porosity with sub- to euhedrally terminated quartz and magnesite (Fig. 7 e). Magnesite dendrites and the interstitial quartz locally have abundant intra-granular nano-porosity (Fig. 7 e).

Discussion

Our results provide strong evidence that ductile deformation structures formed in serpentinites and during the carbonation reaction from serpentinite to listvenite. The structures in listvenites are different from those in carbonate-free serpentinite (Fig. 8) and, as outlined in the following, must have formed during the reaction. We infer a general trend from early ductile deformation to conditions at the brittle-ductile transition (this paper), followed by brittle overprinting after listvenite formation by cataclasis, faulting and veins [38]. Observations in serpentinites of Hole BT1B indicate a similar transition from ductile to brittle deformation over time (Fig. 8).

The earliest preserved deformation microstructures in serpentinite and listvenite are relicts of elongate Cr-spinel and a shape preferred orientation of elongate pseudomorphs of orthopyroxene (bastites), which suggest that parts of the protolith peridotite had a high-temperature porphyroclastic to mylonitic fabric, a common feature of the “Banded Unit” comprising the lowest few kilometers of the mantle section of the Oman ophiolite [45, 46, 47]. This early, pseudomorphosed fabric predates serpentinization and carbonation and in places defines a foliation in listvenite. Serpentinization likely preceded carbonation, because there are 1 – 10 m wide, fully hydrated serpentinite zones between listvenite and partially serpentinized peridotite[18], and because Fe-oxides in listvenite commonly trace a former mesh texture that is typical of serpentinization of olivine [32]. Although direct replacement of olivine or pyroxene by carbonate and quartz may have occurred in places, these observations suggest that most peridotites were fully hydrated before carbonation [32]. Therefore, we infer that the low temperature reaction sequence in the Oman listvenites was (Fig. 9):

(I) serpentinization of olivine and pyroxene,
(II) incipient carbonate formation in serpentinite (“ophicarbonate”),
(III) continued carbonate growth and local replacement of serpentine by quartz and/or amorphous silica (serpentine-magnesite-quartz disequilibrium assemblages),
(IV) full replacement of remnant serpentine by quartz and dendritic carbonate.

An intermediate reaction step forming talc-magnesite assemblages, which is common in many other listvenite occurrences [16, 20, 48] and predicted by modelling [33, 49], is rare in outcrops. In drill core from Hole BT1B, some talc is present in dm – m scale transitions between serpentinite and listvenite [32]. The rare occurrence of talc-bearing assemblages may be attributed to low temperature, a narrow range of water/rock ratios in which talc was stable during carbonation and serpentinization, and/or large disequilibrium of reaction [18, 33, 34]. Some silica may have initially precipitated as opal [32], similar to low-temperature listvenites elsewhere (e.g., [50, 51]), followed by dehydration and recrystallization to quartz or chalcedony. The different reaction stages I to IV likely were active in several simultaneous but spatially separated alteration fronts.

The SPO and CPO in foliated serpentinite likely formed at P–T conditions similar to those of listvenite formation, as indicated by the presence of flattened mesh textures and the predominance of the low-T serpentine polytype lizardite. Ductile deformation of lizardite by basal glide of serpentine [42] (Fig. 2) was thus possibly coeval to the reaction stages producing the ductile deformation structures in listvenite.

Microstructures in foliated listvenites demonstrate that semi-brittle to ductile deformation occurred not only in the precursor serpentinite but also during reaction stages II and III (Fig. 9). The texturally earliest carbonate is Fe-magnesite in the interstices of fragmented Cr-spinel. The spinel fragments are locally rotated (Fig. 3), indicating that the earliest carbonation stage was concomitant with deformation. The formation of early, Fe-bearing magnesite veins followed, indicating that initially fluid flow was focused along fractures, with minor distributed flux causing the precipitation of Fe-magnesite that formed the cores of aligned carbonate ellipsoids (stage II in Fig. 9).

Deformation of the carbonate-bearing, reacting serpentine matrix subsequently led to folding and transposition of the early magnesite veins (Fig. 5) and the development of an axial planar cleavage. Boudinage of Cr-spinel with magnesite precipitation in the necks (Fig. 3) and bending of the foliation around spinel porphyroclasts likely occurred during this phase. Subsequent carbonation under variably supersaturated conditions caused the growth of magnesite ellipsoids with partially euhedral rims in the serpentine matrix. Dendritic magnesite-quartz intergrowths and botryoidal and zoned quartz overgrow all previous (variably deformed) magnesite generations (Fig. 7), suggesting that static, oriented crystal growth prevailed in the final reaction step IV.

Thus, the inferred deformation-reaction relationships indicate that one or several stages of the carbonation reaction were concomitant with distributed deformation. This poses the question whether external stress and related strain enhances fluid flow and the carbonation reaction progress, and whether the observed deformation structures are the inherent consequence of the rheological changes related to the transformation from peridotite to serpentinite and listvenite.

Dislocation creep is commonly inferred to be the most important process forming mineral fabrics. However, crystal plastic deformation is not the only mechanism that can form a CPO. Case studies and experiments on mafic rocks indicate that a CPO may also form by preferential crystal growth and dissolution-precipitation creep during metamorphic reactions [12, 52, 53, 54, 55]. Dissolution-precipitation creep (also referred to as pressure solution, or fluid-assisted diffusion creep) is particularly relevant in presence of high fluid pressure and in porous, fine-grained polyphase assemblages [12, 56, 57]. These conditions are prevalent during metamorphic devolatilization reactions and metasomatic fluid-rock interaction. Thus, dissolution-precipitation creep may often be the dominant deformation mechanism, and the main cause for formation of a CPO and substantial transient weakening in reacting assemblages [29, 53, 58].

Our results point to dissolution-precipitation creep and oriented crystal growth during reaction-assisted, transient weakening of the porous reacting mass as the main cause for the shape and crystallographic preferred orientations in the Oman listvenites: (i) Crosscutting relationships show that the first stages of carbonation were synkinematic (Fig. 3). (ii) Distributed deformation was absent during the final crystallization of dendritic magnesite rims (Fig. 7). (iii) Dislocation densities are low. And (iv), low-angle boundaries formed as nano-scale, intragranular fractures sealed by precipitation (Fig. 6), are inherited from initial growth of nearly parallel crystals perpendicular to vein boundaries, or have radial patterns that also occur in non-foliated listvenite, where they have been interpreted as the result of sector zonation or crystal growth competition [34]. These results exclude dislocation creep as the main deformation mechanism for magnesite in foliated listvenite. Similarly, the common growth zoning and the presence of crystal facets in pores (Fig. 7) are evidence against deformation of quartz by dislocation creep.

Observations from flow-through carbonation experiments suggest that the fluid flow rate and permeability structure has a strong influence on the crystallographic orientation of carbonate, with the fast-growing crystallographic directions ([1014] and [0001]) preferentially oriented normal to the fluid flow direction [59]. Based on the SPO and CPO of lizardite in foliated serpentinites adjacent to listvenites at Site BT1 we infer that fluid flow was commonly anisotropic during the initial stages of carbonation, with higher permeability parallel to the foliation plane. Thus, the CPO of magnesite in foliated listvenites may be due to preferential growth of matrix magnesite, with [1014] and [0001] normal to fluid flow in the foliation plane. Assuming that the SPO of matrix magnesite in foliated listvenite reflects the orientation of a previous serpentine foliation, the expected preferential growth direction is consistent with the measured CPOs of [0001] and [1014] in magnesite (Fig. 4; [1014] is not shown, its orientation and strength of CPO is similar to [0001]). The locally observed CPO of quartz may have formed through a similar process of epitaxial, oriented growth. Alternatively, the CPO of quartz may be inherited from initially present opal or could have formed during dehydration of opal to quartz.

We infer that the transformation of a serpentinized peridotite precursor to carbonate-bearing serpentinite and listvenite is related to changes in rheology due to the changing proportions of olivine/pyroxene, serpentine, magnesite and quartz (± opal), the evolution of porosity, and the different strength of these minerals. Microstructural analysis of the early carbonate generations suggest that once formed, magnesite was stronger than the serpentine matrix. This is manifested in the preserved euhedral magnesite cores, transposition of magnesite veins in a sheared matrix, and folding of magnesite veins while the (inferred) matrix serpentine formed an axial planar cleavage (Fig. 5). Vein microstructures showing small offsets of the growth zoning and a high abundance of low-angle boundaries oriented subparallel to the fold axial plane suggest that grain boundary sliding in the carbonate veins was the main mechanism accommodating folding, while basal glide of serpentine[42] and dissolution-precipitation accommodated deformation in the reacting matrix. Folding was possibly aided by a pre-existing antitaxial, fibrous vein microstructure, where grain boundaries at high angle to the vein walls were oriented favorably for sliding during shortening.

As reviewed in the introduction, the complete reaction sequence requires large fluid - rock ratios and significant porosity. The preserved porosity in the matrix of foliated listvenite (~0.23%) is about one order of magnitude lower than in serpentinite (2.7 ± 1.0 %)[34]. However, locally, inter-granular micro-porosity is abundant in foliated listvenite (Fig. 7 e). Together with intra-granular nano-cracks (Fig. 6) and trans-granular fractures now sealed by magnesite veins, these observations point to a dynamically evolving permeability network at lithostatic fluid pressure that allowed pervasive fluid flow and complete carbonation. We infer that lithostatic pore pressures during serpentinite carbonation in turn promoted ductile deformation in the reacting medium, mainly through grain boundary sliding accommodated by dilatant granular flow and dissolution-precipitation.

Locally, listvenite formation could proceed without apparent finite strain; much of core BT1B consists of non-foliated listvenite containing pseudomorphs after mesh and bastite, enclosing a few bands of non-foliated serpentinite with preserved mesh and bastite textures. In those cases, the pre-existing permeability structure of the serpentinite mesh – deformed in a dilatant fashion under lithostatic pore pressure – may have been the main factor controlling reaction progress. Here we note that in a shear zone, while strain can be strongly localized, shear stress tends to be less heterogeneous, and strain (e.g., 10 %), which can create significant dilatant porosity, would not be visible in the resulting microstructure.

Although they are volumetrically less abundant, shear zones and early magnesite veins are widespread, and may have acted as conduits for advective fluid flow that also supplied CO_2 for the formation of non-foliated listvenite intervals. The strength contrasts between magnesite, quartz/opal and serpentine minerals, and between serpentinite and listvenite likely played a key role in generating locally high differential stress, and in maintaining a high permeability at the reaction front. The conversion of serpentinite into a polyphase, carbonate-serpentine assemblage has two consequences: upon deviatoric stress, pressure solution of serpentine may be enhanced at the interface with the stronger magnesite, and a higher permeability can be expected at un-sealed magnesite veins. Carbonate growth on fold hinges of magnesite veins (Fig. 5 a & b) may be due to this effect. On a larger scale, we propose that the permeability and strength difference between serpentinite and fully reacted and compacted listvenite caused reactive fluids to accumulate along the lithological boundary (i.e. the carbonation reaction front). This may explain why the Oman listvenites consist of a few major bands of 10s of meter thickness that are continuous over long distance, with only rare veins of “listvenite” composition (quartz-magnesite) in serpentinite, and very few non-reacted serpentinite domains within listvenite. In contrast, non-reacted serpentinite relicts within the carbonation reaction product are common during the formation of magnesite-talc rocks in other localities [16, 20]. This suggests that the strength contrast between talc-magnesite and serpentinite is related to a different morphology and permeability profile of the reaction front in comparison to the direct replacement of serpentinite by listvenite, which is related to reaction hardening. Mechanically weaker serpentinite inclusions in a hardening listvenite matrix will preferentially deform and react under tectonic stress. Because the reaction product listvenite is stronger than the serpentine-bearing, fluid-saturated reacting mass, deformation may have been preferentially partitioned in the reacting mass, locally enhancing transient fluid flow and, thus, the carbonation reaction progress.

At the conditions at the base of the Oman ophiolite, high pore pressures may be caused by compaction and dehydration reactions in underlying units [35, 60]. Upon infiltration into mantle rocks a serpentinization front develops. Because of the volume increase of serpentinization, under external stress this is likely to cause cyclic variations in permeability, pore pressure and differential stress, which may induce fracturing and the formation of serpentine and early carbonate veins. The formation of listvenite may intensify this process due to its lower permeability and higher strength compared to serpentinite, causing dilatancy by granular flow and reaction-assisted ductile deformation along the reacting lithological boundary. We speculate that this feedback of external stress, changing rheology and high pore pressure helps to facilitate continued reaction to listvenite despite volume increase, as long as CO_2 supply is sufficiently high.

We propose that similar conditions with external tectonic stress and a rheological feedback enhancing fluid flow and reactivity are likely to be found in most listvenite occurrences worldwide, and may be common in subduction zones and other fluid-rich settings like oceanic transform faults. Hence, reaction-assisted ductile deformation during fluid-rock interaction is likely an important deformation mechanism in subduction zones worldwide, and could explain observed aseismic creep in some regions [61].

Methods

Samples

Samples were collected onboard R/V Chikyu in September 2017 during the Oman drilling Phase 1 core logging and during a field campaign in January 2020, covering the broad and diverse range of (micro)structures in serpentinites and listvenites [32, 33]. After detailed inspection of the core of Hole BT1B, and study of 115 thin sections of selected representative samples, for this study we used a set of 15 listvenite and 6 serpentinite thin sections lacking late overprinting and containing representative ductile deformation structures for detailed investigation (Fig. 1; Supplementary Table S1). Because the penetrative foliation is usually not clearly visible macroscopically, it was not practical to prepare thin sections in the standard structural reference frame. Thus, shear sense indicators like spinel or carbonate sigma-clasts are only well visible in thin sections where the arbitrary core reference frame used to cut samples [62] is coincidently oriented similar to the ideal structural orientation with the section perpendicular to foliation and parallel to a lineation or transport direction. Such features are therefore likely more common than observed.

Optical and scanning electron microscopy (SEM)

Thin sections were scanned in plane-polarized light, reflected light, and at 10 different crossed polarizer orientations with a 10x objective using a PetroScan Virtual Microscope. The PetroScan system is a high-end polarization microscope equipped with a camera and automated sample stage, developed by RWTH Aachen University and Fraunhofer Institute for Applied Information Technology (FIT). During image post-processing, the extinction behavior of each pixel was extracted and interpolated to visualize the extinction behavior at all polarization angles. The high-resolution digital mosaics were used as a reference layer for images acquired by optical CL and scanning electron microscopy, and for image analysis using ImageJ software. A selection of digitized thin sections analyzed in this study are available in the ICDP data repository of the Oman Drilling Project (https://www.icdp-online.org/projects/world/asia/oman/details/).

CL can reveal textures that are not visible using any other imaging method. Variations in CL are caused by natural defects in mineral crystal lattices (vacancies, dislocations) as well as changes in the presence and concentration of trace element and rare-earth element activators [44, 63]. In the case of magnesite, CL is mainly controlled by Mn and Fe contents; Mn^{2+} activates luminescence, whereas Fe acts as a quencher so that magnesite with high Fe (> 7.5 mol% $FeCO_3$) is non-luminescent [64]. Variations in the concentration of Fe, Mn and trace elements thus can cause variations in the luminescence intensity and color, making CL a useful tool to track the evolution of crystal growth recorded in single grains and grain aggregates [44]. In quartz, luminescence depends mainly on structural defects in the crystal lattice and minor substitution of silica tetrahedral by AlO_4M^+ [65]. Because of the potential of this method to reveal key microtextures, we used two complementary modes of CL imaging for this study. Optical mosaic panorama images of large thin section areas were obtained with a Zeiss Axio Scope optical microscope equipped with a “cold” cathode luminoscope CL8200 MK5-2 operating at 15 kV, 320 – 350 µA. Single images were taken with a 10x objective and exposure times of 10 s. Panchromatic and blue-filtered SEM-CL images were acquired using a Zeiss Sigma High Vacuum field emission (FE) scanning electron microscope (SEM) equipped with a Gatan MonoCL4 system at the University of Texas at Austin. Carbon-coated samples were imaged at accelerating voltages of 5 kV, 120 µm aperture, 125 µs dwell time, and 2048 x 2048 pixel resolutions at magnifications up to 2500x following the guidelines of Ukar and Laubach [66].

For phase identification and imaging of chemical zoning, back-scattered electron (BSE) and energy-dispersive X-ray spectroscopy (EDS) large-area maps were acquired with the Zeiss Sigma as well as a Zeiss Gemini SUPRA 55 field-emission electron microscope at the Institute of Tectonics and Geodynamics of RWTH Aachen University. Whole thin sections and areas of interest were mapped with dwell times of 0.2 – 1.5 ms/point at 15 kV and 8.5 mm working distance. High-resolution secondary electron (SE) images were acquired at 3 kV, 5 mm working distance and 20.000 – 30.000x magnification. For conductivity, all samples were coated with a 6 – 8 nm thick layer of tungsten.

Electron backscatter diffraction (EBSD) maps were acquired on areas of interest in thin sections (up to 5 mm^2) using a Zeiss Gemini SEM 300 instrument equipped with an Oxford Symmetry EBSD system at the Central Facility for Electron Microscopy, RWTH Aachen University. Analyses were carried out under variable pressure conditions using N_2 at 30Pa on samples that were tilted 70° at working distances of c. 10 mm, using an accelerating voltage of 20 kV, probe currents of approx. 18nA, and 0.5 – 3 µm step sizes. Data were indexed with Aztec analytical software using the ICSD reference database. Post-processing with Oxford Instruments HKL Channel 5 software included the removal of wild spikes, successive filling of non-indexed pixels according to 8, 7 and 6 neighboring pixel orientations, and the correction of non-systematic misindexation between dolomite and magnesite based on simultaneously acquired EDS data. The Matlab-toolbox MTEX (version 5.3.1) [67] was used for grain boundary modelling (10° segmentation angle), small grains removal (10 pixel threshold), calculation of orientation distribution functions, and for plotting orientation maps and pole figures. Kernel average misorientation maps were calculated with a first order kernel of neighboring pixels in a square. Because thin sections were not prepared in the standard structural reference frame, orientation maps and pole figures are plotted in the arbitrary spatial reference frame of the individual measurement areas within the thin sections (the thin section orientations relative to the core reference frame are given in the supplementary figures).

Micro-computer tomography (micro-CT)

A micro-tomography scan of a foliated listvenite (sample BT1B_14-3_65-66) was acquired from a volume in a 2 x 2 x 13 mm prism oriented in the core reference frame, using an X-Ray Microscope Zeiss Xradia Versa 520 at the MAPEX Center for Materials and Processes, University of Bremen. The micro-CT scan was obtained at 1.3 µm voxel resolution in propagation phase contrast mode, which allows the distinction of quartz and magnesite despite their similar X-ray attenuation. Measurements without propagation phase contrast yielded too low attenuation contrasts between magnesite and quartz. Because this method enhances the contrast at phase boundaries, classical segmentation based on the X-ray attenuation alone could not be applied. Here we used the trainable Weka segmentation 3D machine learning algorithm of ImageJ [68] for phase segmentation in subvolumes of the micro-CT data. The FastRandomForest classifier was applied using the original image and mean, variance, edges and derivatives filters (maximum sigma 8) as training features. The classifier training was repeated once after manual adjustment of classes. This approach produced a reasonable segmentation of quartz-magnesite phase boundaries, but interiors of larger grains were not segmented well. Original and segmented volume renderings are provided in Supplementary figure S6.

Transmission electron microscopy (TEM, STEM)

To gain insights into the nature of low-angle boundaries in matrix magnesite and their possible relation to the deformation microstructures and the observed CPOs, we prepared several 80 – 100 nm thin TEM lamellae by FIB milling from selected magnesite grains along different crystallographic orientations and across low-angle boundaries (Supplementary Fig. S20). The electron transparent specimen preparation for TEM studies were carried out using a dual beam scanning electron microscope (Thermo Fisher Helios 400) equipped with a focused Ga ion beam system. A carbon protective layer was used to protect the specimen from ion sputtering at 30 and 5 kV acceleration voltages. The TEM lamellae were attached to a standard Omniprobe support grid made of Cu. Conventional imaging and electron diffraction studies were carried out using a standard transmission electron microscope (Thermo Fisher Tecnai G2) operated at 200 kV. Chemical composition sensitive scanning TEM (STEM) imaging and measurements were obtained using an electron probe aberration corrected transmission electron microscope (Thermo Fisher Titan 80-200) operated at 200 kV and equipped with an in-column energy dispersive X-ray spectrometry (EDS) detectors. Spectrum imaging using STEM and EDS signals was collected and processed using Velox software (Thermo Fisher). Specimens were aligned and controlled using double tilt TEM holders.

References

1. Halls C, Zhao R. Listvenite and related rocks: perspectives on terminology and mineralogy with reference to an occurrence at Cregganbaun, Co. Mayo, Republic of Ireland. *Mineralium Deposita* **30**, 303-313 (1995).

2. Kelemen PB, Matter J, Streit EE, Rudge JF, Curry WB, Blusztajn J. Rates and Mechanisms of Mineral Carbonation in Peridotite: Natural Processes and Recipes for Enhanced, in situ CO_2 Capture and Storage. In: *Annual Review of Earth and Planetary Sciences, Vol 39* (eds Jeanloz R, Freeman KH) (2011).

3. Kelemen PB, McQueen N, Wilcox J, Renforth P, Dipple G, Vankeuren AP. Engineered carbon mineralization in ultramafic rocks for CO_2 removal from air: Review and new insights. *Chemical Geology*, 119628 (2020).

4. Kelemen PB, Manning CE. Reevaluating carbon fluxes in subduction zones, what goes down, mostly comes up. *Proceedings of the National Academy of Sciences* **112**, E3997-4006 (2015).

5. Guillot S, Schwartz S, Reynard B, Agard P, Prigent C. Tectonic significance of serpentinites. *Tectonophysics* **646**, 1-19 (2015).

6. Schlaphorst D*, et al.* Water, oceanic fracture zones and the lubrication of subducting plate boundaries-insights from seismicity. *Geophysical Journal International* **204**, 1405-1420 (2016).

7. Behr WM, Bürgmann R. What's down there? The structures, materials and environment of deep-seated slow slip and tremor. *Philosophical Transactions of the Royal Society A: Mathematical, Physical and Engineering Sciences* **379**, 20200218 (2021).

8. Burkhard M, Kerrich R, Maas R, Fyfe WS. Stable and Sr-isotope evidence for fluid advection during thrusting of the glarus nappe (swiss alps). *Contributions to Mineralogy and Petrology* **112**, 293-311 (1992).

9. Angiboust S, Pettke T, De Hoog JCM, Caron B, Oncken O. Channelized Fluid Flow and Eclogite-facies Metasomatism along the Subduction Shear Zone. *Journal of Petrology* **55**, 883-916 (2014).

10. Wintsch RP, Christoffersen R, Kronenberg AK. Fluid-rock reaction weakening of fault zones. *Journal of Geophysical Research: Solid Earth* **100**, 13021-13032 (1995).

11. Sibson RH. Structural permeability of fluid-driven fault-fracture meshes. *Journal of Structural Geology* **18**, 1031-1042 (1996).

12. Wassmann S, Stöckhert B. Rheology of the plate interface — Dissolution precipitation creep in high pressure metamorphic rocks. *Tectonophysics* **608**, 1-29 (2013).

13. Rubie DC. Reaction-enhanced ductility: The role of solid-solid univariant reactions in deformation of the crust and mantle. *Tectonophysics* **96**, 331-352 (1983).

14. Okazaki K, Burdette E, Hirth G. Rheology of the Fluid Oversaturated Fault Zones at the Brittle-Plastic Transition. *Journal of Geophysical Research: Solid Earth* **126**, e2020JB020804 (2021).

15. Hansen LD, Dipple GM, Gordon TM, Kellett DA. Carbonated serpentinite (listwanite) at Atlin, British Columbia: A geological analogue to carbon dioxide sequestration. *Canadian Mineralogist* **43**, 225-239 (2005).

16. Menzel MD*, et al.* Carbonation of mantle peridotite by CO_2-rich fluids: the formation of listvenites in the Advocate ophiolite complex (Newfoundland, Canada). *Lithos* **323**, 238-261 (2018).

17. Qiu T, Zhu Y. Listwaenite in the Sartohay ophiolitic mélange (Xinjiang, China): A genetic model based on petrology, U-Pb chronology and trace element geochemistry. *Lithos* **302-303**, 427-446 (2018).

18. Falk ES, Kelemen PB. Geochemistry and petrology of listvenite in the Samail ophiolite, Sultanate of Oman: Complete carbonation of peridotite during ophiolite emplacement. *Geochimica et Cosmochimica Acta* **160**, 70-90 (2015).

19. Nasir S*, et al.* Mineralogical and geochemical characterization of listwaenite from the Semail Ophiolite, Oman. *Geochemistry* **67**, 213-228 (2007).

20. Beinlich A, Plümper O, Hövelmann J, Austrheim H, Jamtveit B. Massive serpentinite carbonation at Linnajavri, N–Norway. *Terra Nova* **24**, 446-455 (2012).

21. Coleman RG, Keith TE. A Chemical Study of Serpentinization—Burro Mountain, California1. *Journal of Petrology* **12**, 311-328 (1971).

22. Klein F, Le Roux V. Quantifying the volume increase and chemical exchange during serpentinization. *Geology* **48**, 552-556 (2020).

23. Kelemen PB, Hirth G. Reaction-driven cracking during retrograde metamorphism: Olivine hydration and carbonation. *Earth and Planetary Science Letters* **345-348**, 81-89 (2012).

24. Malvoisin B, Zhang C, Müntener O, Baumgartner LP, Kelemen PB, Oman Drilling Project Science P. Measurement of Volume Change and Mass Transfer During Serpentinization: Insights From the Oman Drilling Project. *Journal of Geophysical Research: Solid Earth* **125**, e2019JB018877 (2020).

25. van Noort R, Wolterbeek TKT, Drury MR, Kandianis MT, Spiers CJ. The force of crystallization and fracture propagation during in-situ carbonation of peridotite. *Minerals* **7**, (2017).

26. Andreani M, Luquot L, Gouze P, Godard M, Hoisé E, Gibert B. Experimental study of carbon sequestration reactions controlled by the percolation of CO_2-rich brine through peridotites. *Environmental Science & Technology* **43**, 1226-1231 (2009).

27. Hövelmann J, Austrheim H, Jamtveit B. Microstructure and porosity evolution during experimental carbonation of a natural peridotite. *Chemical Geology* **334**, 254-265 (2013).

28. Fusseis F, Regenauer-Lieb K, Liu J, Hough RM, De Carlo F. Creep cavitation can establish a dynamic granular fluid pump in ductile shear zones. *Nature* **459**, 974-977 (2009).

29. Urai JL, Feenstra A. Weakening associated with the diaspore–corundum dehydration reaction in metabauxites: an example from Naxos (Greece). *Journal of Structural Geology* **23**, 941-950 (2001).

30. Laubach SE*, et al.* The Role of Chemistry in Fracture Pattern Development and Opportunities to Advance Interpretations of Geological Materials. *Reviews of Geophysics* **57**, 1065-1111 (2019).

31. Spruženiece L, Späth M, Urai JL, Ukar E, Selzer M, Nestler B. Wide-blocky veins explained by dependency of crystal growth rate on fracture surface type: Insights from phase-field modeling. *Geology*, (2021).

32. Kelemen PB, Matter JM, Teagle DAH, Coggon JA, and the Oman Drilling Project Science Team. Site BT1: fluid and mass exchange on a subduction zone plate boundary. In: *Proceedings of the Oman Drilling Project* (eds Kelemen PB, Matter JM, Teagle DAH, Coggon JA, et al.). International Ocean Discovery Program (2020).

33. Kelemen PB*, et al.* Mass transfer into the leading edge of the mantle wedge: Initial Results from Oman Drilling Project Hole BT1B. *Journal of Geophysical Research*, (in review).

34. Beinlich A*, et al.* Ultramafic Rock Carbonation: Constraints From Listvenite Core BT1B, Oman Drilling Project. *J Geophys Res-Sol Ea* **125**, e2019JB019060 (2020).

35. Grobe A, *et al.* Tectono-thermal evolution of Oman's Mesozoic passive continental margin under the obducting Semail Ophiolite: a case study of Jebel Akhdar, Oman. *Solid Earth* **10**, 149-175 (2019).

36. Kotowski AJ, Cloos M, Stockli DF, Orent EB. Structural and thermal evolution of an infant subduction shear zone: Insights from sub-ophiolite metamorphic rocks recovered from Oman Drilling Project Site BT-1B. Preprint at https://doi.org/10.1002/essoar.10505943.1 (2021).

37. Searle MP, Cox JON. Subduction zone metamorphism during formation and emplacement of the Semail ophiolite in the Oman Mountains. *Geological Magazine* **139**, 241-255 (2002).

38. Menzel MD*, et al.* Brittle Deformation of Carbonated Peridotite—Insights From Listvenites of the Samail Ophiolite (Oman Drilling Project Hole BT1B). *Journal of Geophysical Research: Solid Earth* **125**, e2020JB020199 (2020).

39. Kelemen PB, Matter JM, Teagle DAH, Coggon JA, and the Oman Drilling Project Science Team. Site BA4. In: *Proceedings of the Oman Drilling Project* (eds Kelemen PB, Matter JM, Teagle DAH, Coggon JA, et al.). International Ocean Discovery Program (2020).

40. Bach W, Garrido CJ, Paulick H, Harvey J, Rosner M. Seawater-peridotite interactions: First insights from ODP Leg 209, MAR 15°N. *Geochemistry, Geophysics, Geosystems* **5**, n/a-n/a (2004).

41. Amiguet E, Van De Moortèle B, Cordier P, Hilairet N, Reynard B. Deformation mechanisms and rheology of serpentines in experiments and in nature. *Journal of Geophysical Research: Solid Earth* **119**, 4640-4655 (2014).

42. Hirauchi K-i, Katayama I, Uehara S, Miyahara M, Takai Y. Inhibition of subduction thrust earthquakes by low-temperature plastic flow in serpentine. *Earth and Planetary Science Letters* **295**, 349-357 (2010).

43. Passchier CW, Trouw RAJ. *Microtectonics*, 2nd edn. Springer (2005).

44. Götze J, Schertl H-P, Neuser RD, Kempe U, Hanchar JM. Optical microscope-cathodoluminescence (OM–CL) imaging as a powerful tool to reveal internal textures of minerals. *Mineralogy and Petrology* **107**, 373-392 (2013).

45. Prigent C, Agard P, Guillot S, Godard M, Dubacq B. Mantle Wedge (De)formation During Subduction Infancy: Evidence from the Base of the Semail Ophiolitic Mantle. *Journal of Petrology* **59**, 2061-2092 (2018).

46. Boudier F, Ceuleneer G, Nicolas A. Shear zones, thrusts and related magmatism in the Oman ophiolite: Initiation of thrusting on an oceanic ridge. *Tectonophysics* **151**, 275-296 (1988).

47. Boudier F, Coleman RG. Cross section through the peridotite in the Samail Ophiolite, southeastern Oman Mountains. *Journal of Geophysical Research: Solid Earth* **86**, 2573-2592 (1981).

48. Boskabadi A*, et al.* Carbonation of ophiolitic ultramafic rocks: Listvenite formation in the Late Cretaceous ophiolites of eastern Iran. *Lithos* **352-353**, 105307 (2020).

49. Klein F, Garrido CJ. Thermodynamic constraints on mineral carbonation of serpentinized peridotite. *Lithos* **126**, 147-160 (2011).

50. Ulrich M*, et al.* Dissolution-precipitation processes governing the carbonation and silicification of the serpentinite sole of the New Caledonia ophiolite. *Contributions to Mineralogy and Petrology* **167**, (2014).

51. Boschi C, Dini A, Dallai L, Ruggieri G, Gianelli G. Enhanced CO_2-mineral sequestration by cyclic hydraulic fracturing and Si-rich fluid infiltration into serpentinites at Malentrata (Tuscany, Italy). *Chemical Geology* **265**, 209-226 (2009).

52. Mansard N, Stünitz H, Raimbourg H, Précigout J, Plunder A, Nègre L. Relationship between microstructures and resistance in mafic assemblages that deform and transform. *Solid Earth* **11**, 2141-2167 (2020).

53. Stünitz H, Neufeld K, Heilbronner R, Finstad AK, Konopásek J, Mackenzie JR. Transformation weakening: Diffusion creep in eclogites as a result of interaction of mineral reactions and deformation. *Journal of Structural Geology* **139**, 104129 (2020).

54. Bons PD, den Brok B. Crystallographic preferred orientation development by dissolution–precipitation creep. *Journal of Structural Geology* **22**, 1713-1722 (2000).

55. Shelley D. Plagioclase and quartz preferred orientations in a low-grade schist: the roles of primary growth and plastic deformation. *Journal of Structural Geology* **11**, 1029-1037 (1989).

56. Kenis I, Urai JL, van der Zee W, Hilgers C, Sintubin M. Rheology of fine-grained siliciclastic rocks in the middle crust—evidence from structural and numerical analysis. *Earth and Planetary Science Letters* **233**, 351-360 (2005).

57. Wheeler J. Importance of pressure solution and coble creep in the deformation of polymineralic rocks. *Journal of Geophysical Research: Solid Earth* **97**, 4579-4586 (1992).

58. Stünitz H, Tullis J. Weakening and strain localization produced by syn-deformational reaction of plagioclase. *International Journal of Earth Sciences* **90**, 136-148 (2001).

59. Peuble S*, et al.* Carbonate mineralization in percolated olivine aggregates: Linking effects of crystallographic orientation and fluid flow. *American Mineralogist* **100**, 474-482 (2015).

60. Audet P, Bostock MG, Christensen NI, Peacock SM. Seismic evidence for overpressured subducted oceanic crust and megathrust fault sealing. *Nature* **457**, 76-78 (2009).

61. Fagereng Å, den Hartog SAM. Subduction megathrust creep governed by pressure solution and frictional–viscous flow. *Nature Geoscience* **10**, 51-57 (2017).

62. Kelemen PB, Matter JM, Teagle DAH, Coggon JA, and the Oman Drilling Project Science Team. Methods and explanatory notes. In: *Proceedings of the Oman Drilling Project* (eds Kelemen PB, Matter JM, Teagle DAH, Coggon JA, et al.). International Ocean Discovery Program (2020).

63. Boggs S, Krinsley D. *Application of cathodoluminescence imaging to the study of sedimentary rocks*. Cambridge University Press (2006).

64. Spötl C. Cathodoluminescence of magnesite:Examples from the Eastern Alps. *Geology* **19**, 52 (1991).

65. Richter DK, Götte T, Götze J, Neuser RD. Progress in application of cathodoluminescence (CL) in sedimentary petrology. *Mineralogy and Petrology* **79**, 127-166 (2003).

66. Ukar E, Laubach SE. Syn- and postkinematic cement textures in fractured carbonate rocks: Insights from advanced cathodoluminescence imaging. *Tectonophysics* **690**, 190-205 (2016).

67. Bachmann F, Hielscher R, Schaeben H. Texture analysis with MTEX- Free and open source software toolbox. In: *Solid State Phenomena* (2010).

68. Arganda-Carreras I*, et al.* Trainable Weka Segmentation: a machine learning tool for microscopy pixel classification. *Bioinformatics* **33**, 2424-2426 (2017).

69. Béchennec F, Roger J, Le Métour J, Wyns R. Geological Map Oman 1 : 250.000, Seeb - Sheet NF40-03. BRGM Orléans France (1992).

70. Nicolas A, Boudier F. Mapping oceanic ridge segments in Oman ophiolite. *Journal of Geophysical Research: Solid Earth* **100**, 6179-6197 (1995).

Acknowledgments

We thank Michael Kettermann and Yumiko Harigane for sampling onboard Chikyu. Werner Kraus and Jonatan Schmidt are thanked for thin section preparation and technical assistance. We thank Wolf Achim Kahl for conducting the micro-CT measurements. We are grateful to the Oman Public Authority of Mining for support to conduct field work and sample export. MDM and JLU acknowledge funding by the German Research Foundation (DFG grant UR 64/20-1). This research used samples and data provided by the Oman Drilling Project. The Oman Drilling Project (OmanDP) has been possible through co-mingled funds from the International Continental Scientific Drilling Project (ICDP), the Sloan Foundation – Deep Carbon Observatory (Grant 2014-3-01), the US National Science Foundation (NSF-EAR-1516300), NASA – Astrobiology Institute NNA15BB02A), the German Research Foundation (DFG: KO 1723/21-1), the Japanese Society for the Promotion of Science (JSPS no:16H06347; and KAKENHI 16H02742), the European Research Council (Adv: no.669972), the Swiss National Science Foundation (SNF:20FI21_163073), the Japanese Marine Science and Technology Center (JAMSTEC), the International Ocean Discovery Program (IODP), and contributions from the Sultanate of Oman Ministry of Regional Municipalities and Water Resources, the Oman Public Authority of Mining, Sultan Qaboos University, CRNS-Univ. Montpellier II, Columbia University of New York, and the University of Southampton.

Author contributions

MDM and JLU designed the study; JLU and PK were involved in sampling; MDM, JLU and PK conducted microstructural analysis by optical microscopy; MDM performed SEM imaging, EDS mapping, optical CL analysis and image and micro-CT processing; EU conducted SEM and SEM-CL analysis; AS and MDM conducted EBSD analysis and data treatment; AK and LK performed FIB preparation, and TEM and STEM analysis. MDM, JLU, PK, GH and EU were involved in extensive discussion and manuscript writing. All authors contributed to the interpretation of data and the manuscript text.

Competing interests

The authors declare no competing interests.

Figure captions

Fig. 1 (a) Simplified geological overview of the northern Samail massif in Northern Oman, with site BT1 indicated, (b) schematic cross-section, and (c) simplified stratigraphy of the Oman ophiolite and underlying units. The map and column are adapted after [69] and [70]. (d) Field view of listvenites and serpentinites close to site BT1. (e) Overview of Hole BT1B (modified from [32]) with the location of studied samples. (f - i) Split core images of (f) foliated and folded listvenite (sample BT1B_21-3_35-40), (g) foliated carbonate-bearing serpentinite (sample BT1B_39-4_14-18), (h) veined shear zone in massive, non-foliated listvenite (sample BT1B_51-1_20-25), and (i) zone of foliated serpentinite cutting non-foliated mesh-bastite textured serpentinite (sample BT1B_74-1_59-62). (j) SEM-CL image showing zoning of magnesite ellipsoids with shape preferred orientation (BT1B_14-3_77-80). (k) BSE image of a magnesite ellipsoid with Fe-oxide inclusions (brightest) and Fe-magnesite cores (BT1B_15-1_32-34). Scale bar in f) - i) is 2 cm, in j) 100 µm and in k) 25 µm.

Fig. 2 Deformation microstructures in serpentinites. (a) Foliated serpentinite with CPO and aligned Fe-oxides tracing former polygonal, now flattened mesh cells (crossed polarized image (xpol) with 1λ-plate; sample OM20-13); (b) Serpentinite mylonite with strong CPO of lizardite and bastite porphyroclast, cut by a later serpentine vein with anomalous extinction color (xpol with 1λ-plate). (c) Grain size reduction in shear bands (GSRZ), and deformation lamellae and kinking (red arrow in c) of larger serpentine grains (xpol). b) and c) are both from sample BT1B_74-1_59-61). Scale bars: 200 µm.

Fig. 3 Boudinage of Cr-Spinel in foliated listvenite. (a) Combined reflected light and xpol with 1λ-plate. (b, c) Mg and Fe chemical maps of the area indicated in a), showing Fe-rich magnesite between spinel fragments and a Fe-bearing seam at the contact between magnesite in the boudin neck and the quartz-magnesite matrix (white arrow). Fe-magnesite in the core of a ellipsoid forms a sigma-clast in the matrix (yellow arrow, σ). (d) SEM-CL image of the same area showing different magnesite generations and growth zonation in quartz. (e) EBSD phase map. (f) Crystallographic orientations of magnesite (inverse pole figure (ipf) color scale: see inset). (g) Crystallographic orientation of chromite fragments (ipf color scale see inset) and kernel average misorientation of magnesite, showing low-angle boundaries in red. (Sample BT1B_14-3_77-80). Scale bars: 75 µm.

Fig. 4 Microstructures in listvenites with penetrative foliation and corresponding contoured pole figures of magnesite and quartz c-axes (1 point per grain; lower hemisphere) in thin section reference (x, y coordinates see inset in a). The black dotted line in pole figures shows the orientation of the foliation trace in thin section based on the elongation direction of magnesite grains; contours are multiples of a random distribution. Pole figures based on all points (not shown) have similar distributions; full pole figures including a- and m- axes see Supplementary figures S8 – S19. (a) ppol; (b) quartz orientations (ipf colorscale see inset), and kernel average misorientation of magnesite grains in grey; (c) xpol with 1λ-plate; (d) BSE image; (e) magnesite orientations (colorscale see inset in b); black = other phases, not indexed). Scale bar in a) is 500 µm, in b) – e) 100 µm.

Fig. 5 Ductile transposition and folding of early magnesite veins. (a) folded magnesite veins, the matrix consists of quartz and aligned magnesite dendrites (xpol with 1λ-plate; BT1B_21-3_35-40). (b) CL image of the same area as in a), showing pink luminescent magnesite overgrowth on folded veins (arrows). In the lower right domain listvenite resembles a mesh texture and veins are not folded. (c) BSE image of transposed magnesite vein with magnesite dendrites growing oblique to the foliation in the opening space (red arrow). In this image the contrast was enhanced and oxides are rendered black (BT1B_20-1_64-68). (d) BSE image of folded magnesite vein, with euhedral magnesite overgrowths on the vein rims (yellow arrows) (BT1B_16-3_28-31). (e) EBSD orientation map of magnesite of the same area as in d) (ipf color scale see inset), with average orientation of magnesite [001] in different vein parts and of quartz [001] in the matrix indicated (c.f. Fig. 4). In a) and d), the trace of the fold axial surfaces and the parallel SPO of dendritic magnesite is marked by the dotted lines. Scale bar in a) and b) is 400 µm, in c) - e) 200 µm.

Fig. 6 Low-angle boundaries in magnesite of foliated listvenite. (a) EBSD kernel average misorientation map of magnesite (3° threshold); the magnesite grain selected for TEM analysis and the orientation of the FIB section are indicated. (b) STEM bright field image of a low-angle boundary (gb*) in the selected magnesite grain, and Fe and Si compositional maps of the framed area. (Sample BT1B_14-3_65-66).

Fig. 7 Crystal growth microstructures in foliated listvenites. (a) SEM-CL image of aligned magnesite ellipsoids with Fe-magnesite (black) cores and aligned magnesite dendrites, in a quartz matrix with euhedral crystal growth zoning (CL filter optimized for quartz). (b) SEM-CL image of magnesite ellipsoids with concentric zoning and dendritic rims, and concentric spherulitic to botryoidal growth zoning of quartz (CL filter optimized for magnesite). (c) Euhedral magnesite with Fe-oxide inclusions and dendritic rims; quartz in the matrix has a CPO (c.f. Fig. 4c) (xpol). (d) EBSD orientation map of magnesite (color scale see Fig. 4) with corresponding crystal shapes overlay of rhombohedral magnesite (crystallographic axes see inset). (e) SE image of dendritic rim on euhedral magnesite. Sub-micron scale crystal facets of quartz and magnesite are visible in the related porosity. (f) High resolution SE image of a nano-porous magnesite dendrite showing a 100 - 400 nm wide SiO_2 rim at the contact to quartz. (a, b: sample BT1B_14-3_77-80; c - f: sample BT1B_16-3_28-31). Scale bars in a) - c) are 50 µm, in d) 200 µm (black bar), in e) 10 µm and in f) 2.5 µm.

Fig. 8 Relative age relations of carbonation reaction and deformation structures in serpentinites and listvenites of core BT1B. Cross-correlation between events in serpentinite relative to those in listvenite is uncertain.

Fig. 9 Schematic mineral growth and deformation evolution during progressive reaction of serpentinite to listvenite in sheared intervals of Hole BT1B.

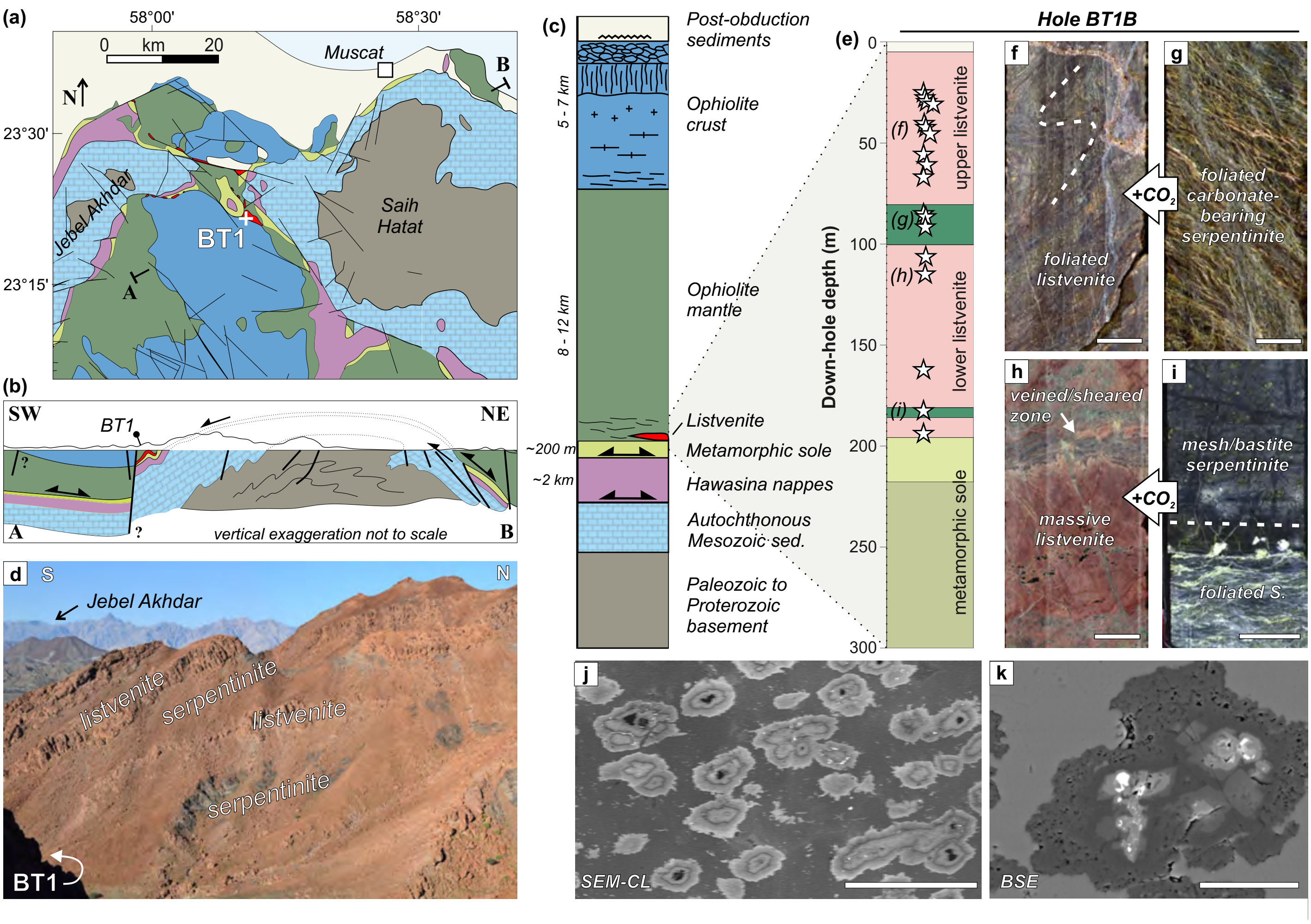

Fig. 1 (a) Simplified geological overview of the northern Samail massif in Northern Oman, with site BT1 indicated, (b) schematic cross-section, and (c) simplified stratigraphy of the Oman ophiolite and underlying units. The map and column are adapted after ref. 69 and 70. (d) Field view of listvenites and serpentinites close to site BT1. (e) Overview of Hole BT1B (modified from ref. 32) with the location of studied samples. (f - i) Split core images of (f) foliated and folded listvenite (sample BT1B_21-3_35-40), (g) foliated carbonate-bearing serpentinite (sample BT1B_39-4_14-18), (h) veined shear zone in massive, non-foliated listvenite (sample BT1B_51-1_20-25), and (i) zone of foliated serpentinite cutting non-foliated mesh-bastite textured serpentinite (sample BT1B_74-1_59-62). (j) SEM-CL image showing zoning of magnesite ellipsoids with shape preferred orientation (BT1B_14-3_77-80). (k) BSE image of a magnesite ellipsoid with Fe-oxide inclusions (brightest) and Fe-magnesite cores (BT1B_15-1_32-34). Scale bar in f) - i) is 2 cm; in j) 100 μm and in k) 25 μm.

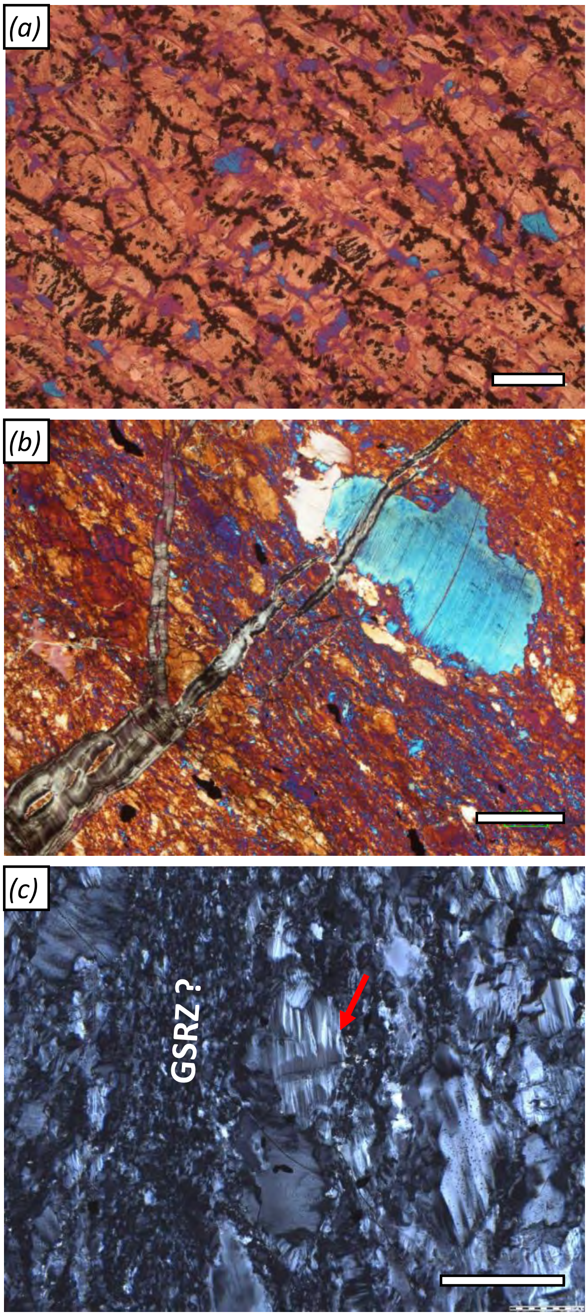

Fig. 2 *Deformation microstructures in serpentinites. (a) Foliated serpentinite with CPO and aligned Fe-oxides tracing former polygonal, now flattened mesh cells (crossed polarized image (xpol) with 1λ-plate; sample OM20-13); (b) Serpentinite mylonite with strong CPO of lizardite and bastite porphyroclast, cut by a later serpentine vein with anomalous extinction color (xpol with 1λ-plate). (c) Grain size reduction in shear bands (GSRZ), and deformation lamellae and kinking (red arrow in c) of larger serpentine grains (xpol). b) and c) are both from sample BT1B_74-1_59-61). Scale bars: 200 µm.*

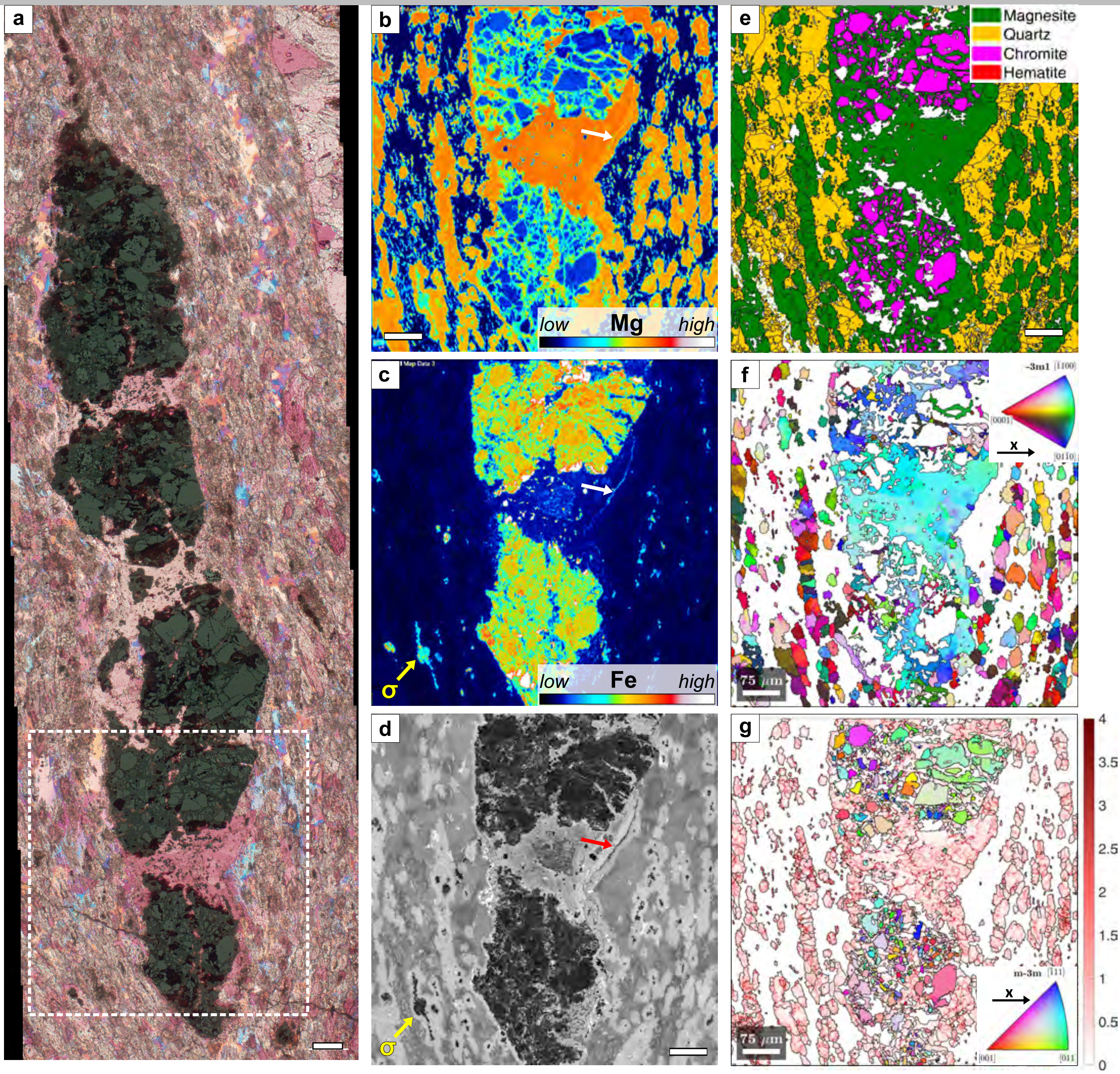

Fig. 3 *Boudinage of Cr-Spinel in foliated listvenite. (a) Combined reflected light and xpol with 1λ-plate. (b, c) Mg and Fe chemical maps of the area indicated in a), showing Fe-rich magnesite between spinel fragments and a Fe-bearing seam at the contact between magnesite in the boudin neck and the quartz-magnesite matrix (white arrow). Fe-magnesite in the core of a ellipsoid forms a sigma-clast in the matrix (yellow arrow, σ). (d) SEM-CL image of the same area showing different magnesite generations and growth zoning in quartz. (e) EBSD phase map. (f) Crystallographic orientations of magnesite (inverse pole figure (ipf) colorscale: see inset). (g) Crystallographic orientation of chromite fragments (ipf colorscale see inset) and kernel average misorientation of magnesite, showing low-angle boundaries in red. (Sample BT1B_14-3_77-80). Scale bars: 75 µm.*

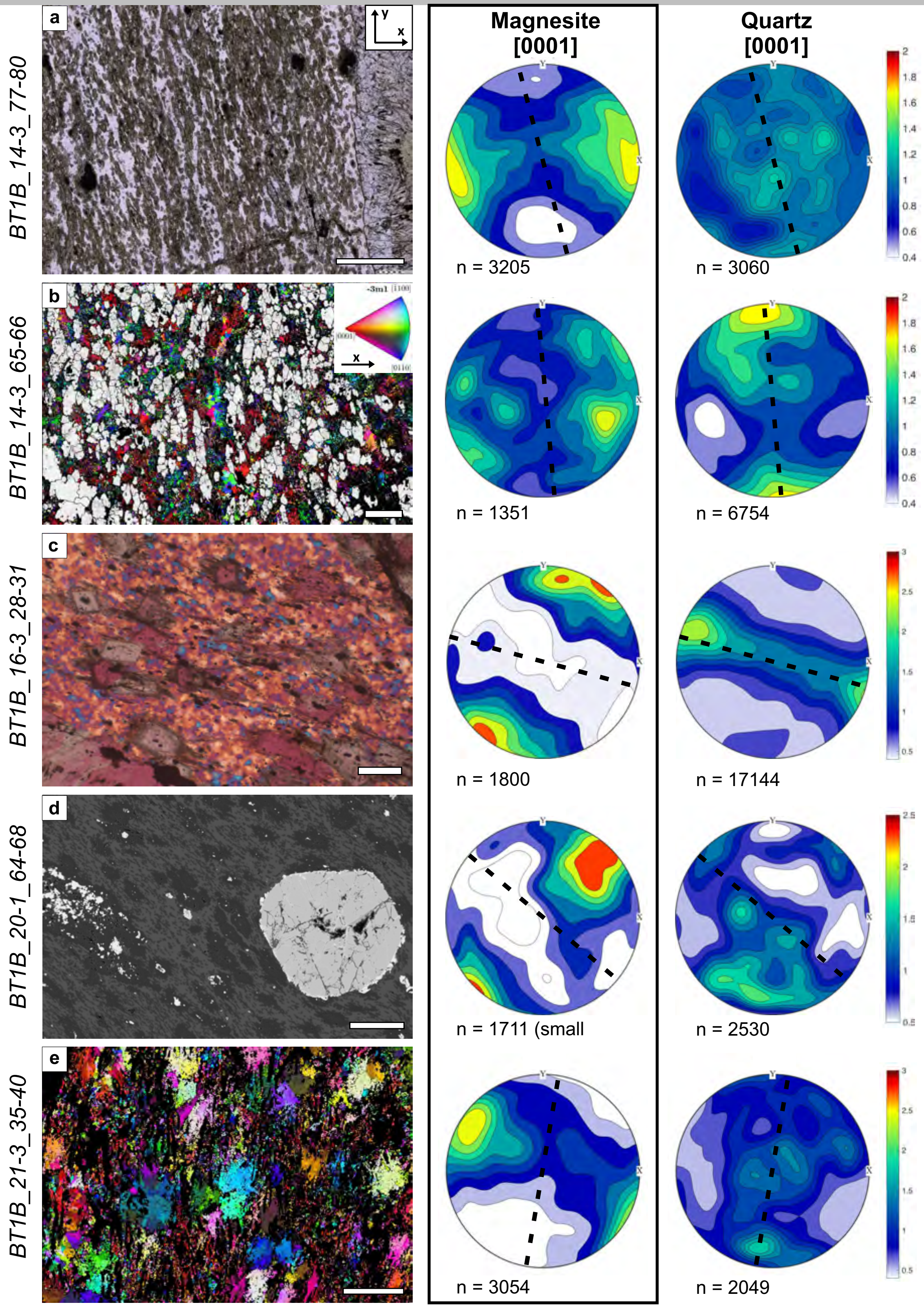

Fig. 4 *Microstructures in listvenites with penetrative foliation and corresponding contoured pole figures of magnesite and quartz c-axes (1 point per grain; lower hemisphere) in thin section reference (x, y coordinates see inset in a). The black dotted line in pole figures shows the orientation of the foliation trace in thin section based on the elongation direction of magnesite grains; contours are multiples of a random distribution. Pole figures based on all points (not shown) have similar distributions; full pole figures including a- and m- axes see Supplementary figures S8 – S19. (a) ppol; (b) quartz orientations (ipf colorscale see inset), and kernel average misorientation of magnesite grains in grey; (c) xpol with 1λ-plate; (d) BSE image; (e) magnesite orientations (colorscale see inset in b); black = other phases, not indexed). Scale bar in a) is 500 μm, in b) - e) 100 μm.*

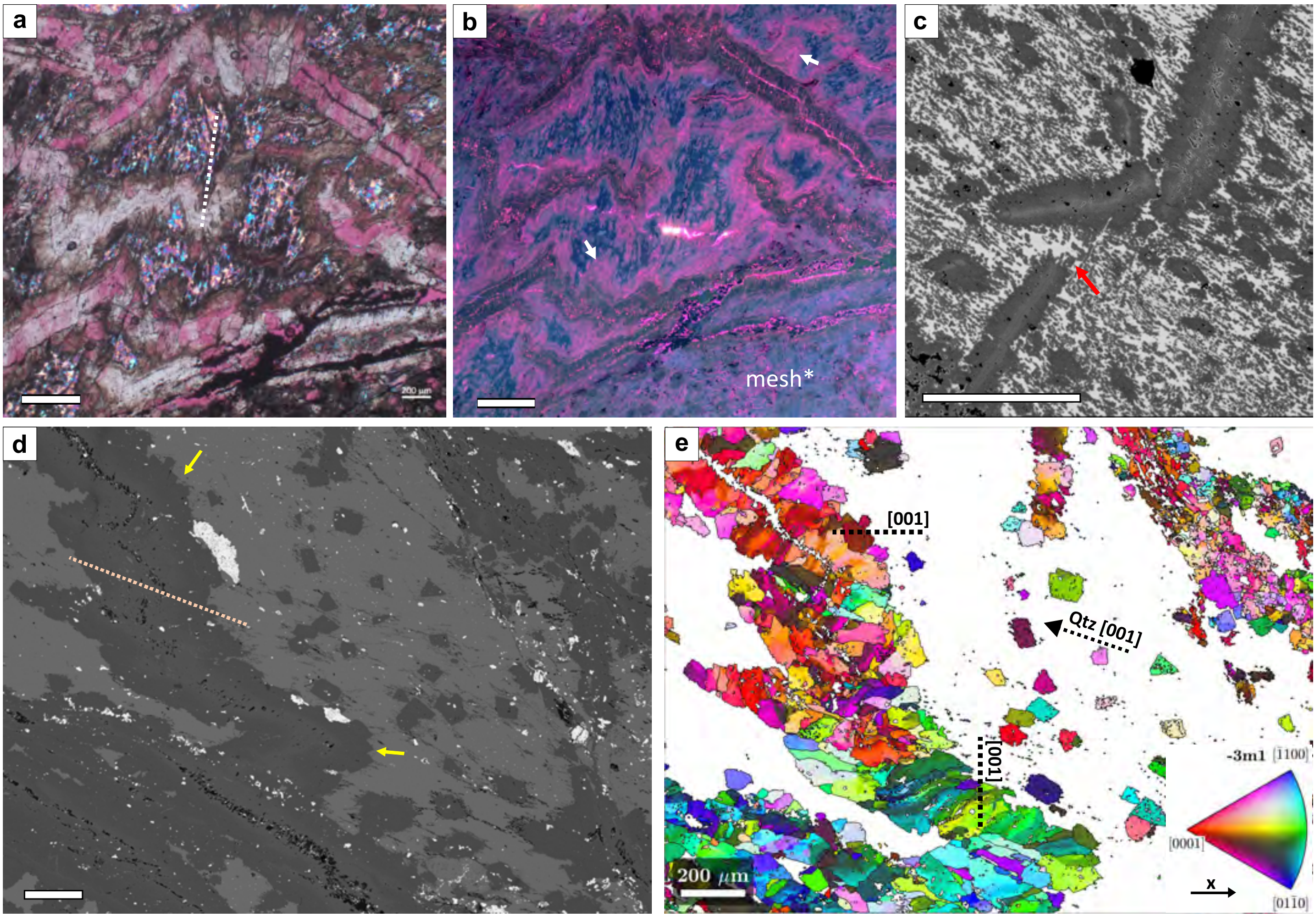

Fig. 5 *Ductile transposition and folding of early magnesite veins. (a) folded magnesite veins, the matrix consists of quartz and aligned magnesite dendrites (xpol with 1λ-plate; BT1B_21-3_35-40). (b) CL image of the same area as in a), showing pink luminescent magnesite overgrowth on folded veins (arrows). In the lower right domain listvenite resembles a mesh texture and veins are not folded. (c) BSE image of transposed magnesite vein with magnesite dendrites growing oblique to the foliation in the opening space (red arrow). In this image the contrast was enhanced and oxides are rendered black (BT1B_20-1_64-68). (d) BSE image of folded magnesite vein, with euhedral magnesite overgrowths on the vein rims (yellow arrows) (BT1B_16-3_28-31). (e) EBSD orientation map of magnesite of the same area as in d) (ipf colorscale see inset), with average orientation of magnesite [001] in different vein parts and of quartz [001] in the matrix indicated (c.f. Fig. 4c). In a) and d), the trace of the fold axial surfaces and the parallel SPO of dendritic magnesite is marked by the dotted lines. Scale bar in a) and b) is 400 μm, in c) - e) 200 μm.*

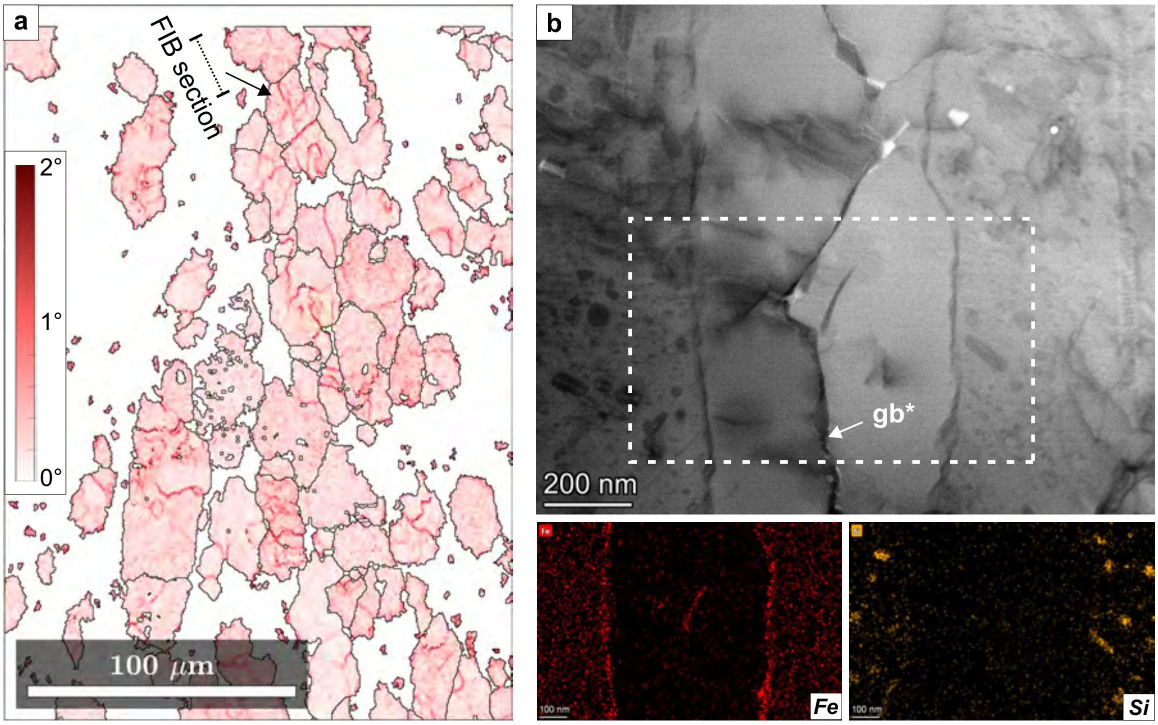

Fig. 6 Low-angle boundaries in magnesite of foliated listvenite. (a) EBSD kernel average misorientation map of magnesite (3° threshold); the magnesite grain selected for TEM analysis and the orientation of the FIB section are indicated. (b) STEM bright field image of a low-angle boundary (gb*) in the selected magnesite grain, and Fe and Si compositional maps of the framed area. (Sample BT1B_14-3_65-66).

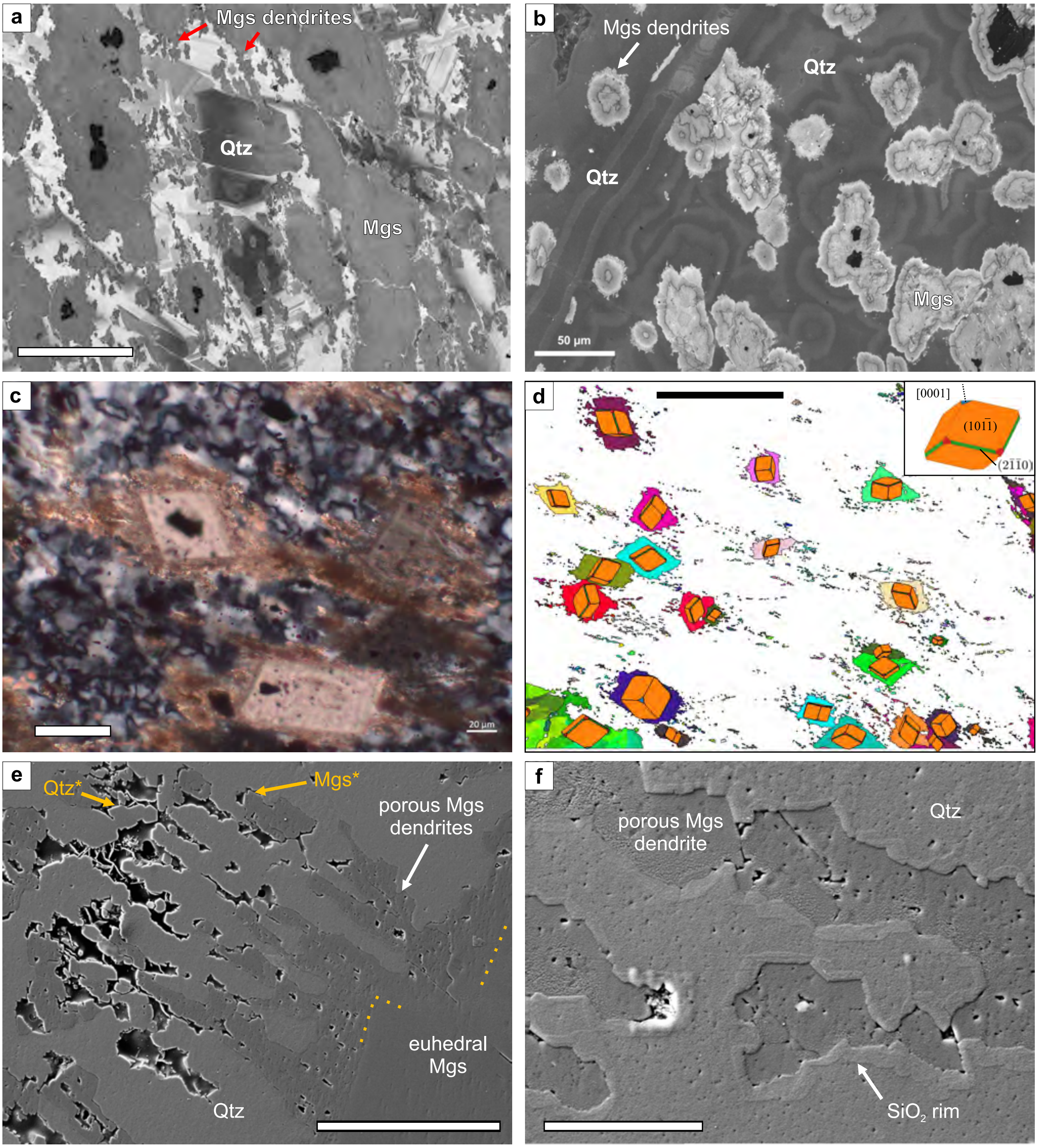

Fig. 7 *Crystal growth microstructures in foliated listvenites. (a) SEM-CL image of aligned magnesite ellipsoids with Fe-magnesite (black) cores and aligned magnesite dendrites, in a quartz matrix with euhedral crystal growth zoning (CL filter optimized for quartz). (b) SEM-CL image of magnesite ellipsoids with concentric zoning and dendritic rims, and concentric spherulitic to botryoidal growth zoning of quartz (CL filter optimized for magnesite). (c) Euhedral magnesite with Fe-oxide inclusions and dendritic rims; quartz in the matrix has a CPO (c.f. Fig. 4c) (xpol). (d) EBSD orientation map of magnesite (colorscale see Fig. 4) with corresponding crystal shapes overlay of rhombohedral magnesite (crystallographic axes see inset). (e) SE image of dendritic rim on euhedral magnesite. Sub-micron scale crystal facets of quartz and magnesite are visible in the related porosity. (f) High resolution SE image of a nano-porous magnesite dendrite showing a 100 - 400 nm wide SiO_2 rim at the contact to quartz. (a, b: sample BT1B_14-3_77-80; c - f: sample BT1B_16-3_28-31). Scale bars in a) - c) are 50 µm, in d) 200 µm (black bar), in e) 10 µm and in f) 2.5 µm.*

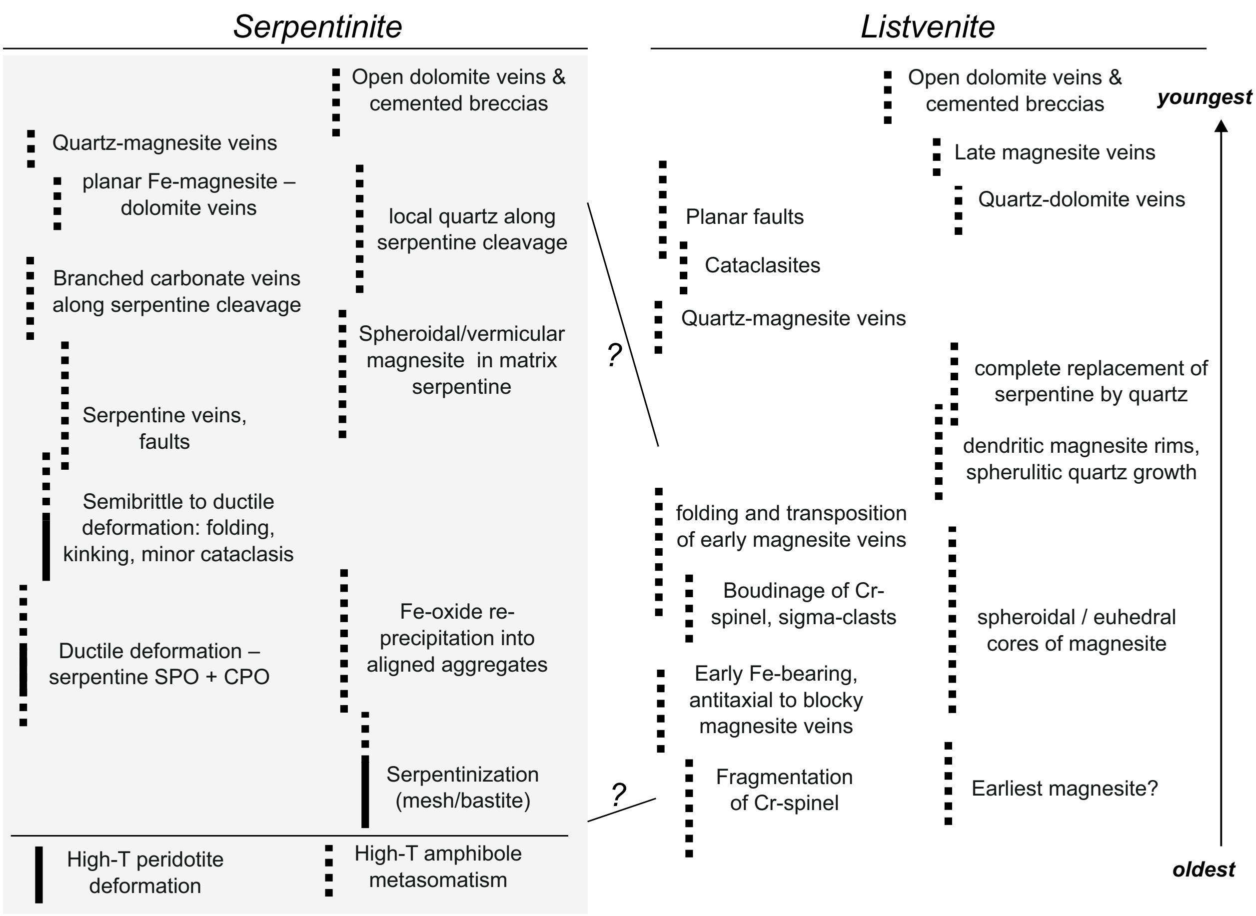

Fig. 8. *Relative age relations of carbonation reaction and deformation structures in serpentinites and listvenites of core BT1B. Cross-correlation between events in serpentinite relative to those in listvenite is uncertain.*

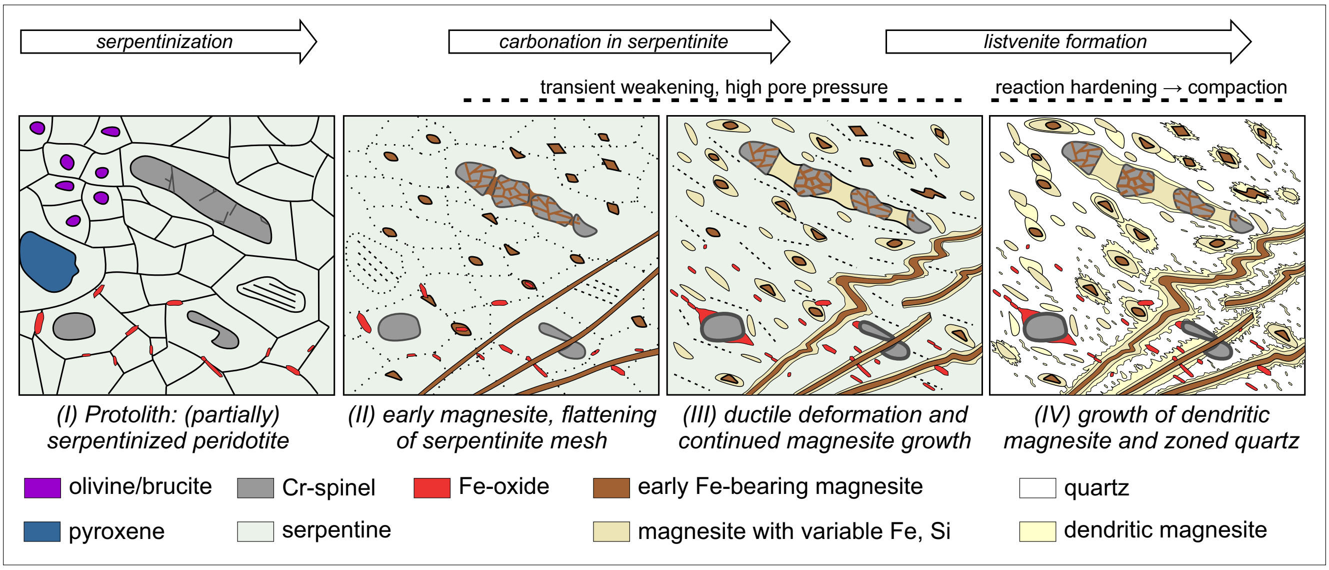

Fig. 9 *Schematic mineral growth and deformation evolution during progressive reaction of serpentinite to listvenite in sheared intervals of Hole BT1B.*